

General simulation method for spontaneous parametric down- and parametric up-conversion experiments

Felix Riexinger^{1,2*}, Mirco Kutas^{1,2}, Björn Haase^{1,2}, Patricia Bickert¹, Daniel Molter¹, Michael Bortz¹, and Georg von Freymann^{1,2}

¹ Fraunhofer Institute for Industrial Mathematics ITWM, Fraunhofer-Platz 1, 67663 Kaiserslautern, Germany

² Department of Physics and Research Center OPTIMAS, Technische Universität Kaiserslautern (TUK), 67663 Kaiserslautern, Germany

* felix.riexinger@itwm.fraunhofer.de

March 8, 2022

1 Abstract

2 Spontaneous parametric down-conversion (SPDC) sources are an important technology
3 for quantum sensing and imaging. We demonstrate a general simulation method, based
4 on modeling from first principles, reproducing the spectrally and spatially resolved abso-
5 lute counts of a SPDC experiment. By additionally simulating parametric up- and down-
6 conversion processes with thermal photons as well as effects of the optical system we
7 accomplish good agreement with the experimental results. This method is broadly ap-
8 plicable and allows for the separation of contributing processes, virtual characterization
9 of SPDC sources, and enables the simulation of many quantum based applications.

10 1 Introduction

11 Entangled and correlated photon pairs have become the basis for many applications in quan-
12 tum optics. They are used in various quantum based schemes such as ghost imaging [1, 2],
13 optical coherence tomography [3], spectroscopy [4, 5], quantum sensing [6], and imaging
14 with undetected photons [7–9]. One of the most prominent methods for generating entan-
15 gled photon pairs is spontaneous parametric down-conversion (SPDC), where a pump laser
16 photon decays into two lower-energy photons in a medium with a second-order nonlinearity.
17 The entanglement can exist in many of the photon properties, such as polarization, wave-
18 length, or momentum, making SPDC a versatile source for entangled photons. Additionally,
19 the process is easy to implement and well understood experimentally. However, an accurate
20 simulation method for SPDC sources is required as the foundation for simulations of many
21 applications with entangled photons. The availability of detailed simulations can help resolve
22 problems such as finding limitations to the resolution or visibility of quantum imaging [8, 9].
23 This issue is becoming more relevant as applications for SPDC sources are on the verge of a
24 breakthrough, but their limiting factors need to be understood better to exploit the full poten-
25 tial of such quantum based applications.

26 The theory of SPDC is well developed and multiple approaches to simulating the proper-
27 ties of the created photons are available [10, 11]. Existing SPDC simulations are tailored for
28 specialized applications limiting their general applicability. The limitations include restriction
29 to the paraxial regime [11, 12] and narrow frequency or wave vector spreads [12–14]. Many
30 works do not predict absolute photon conversion rates [12–16]. In this letter we propose and
31 demonstrate a novel simulation method for SPDC sources and the subsequent measurement

32 setup. The sparse use of approximations makes the underlying model applicable to a wide
 33 range of SPDC sources from the ultraviolet to the terahertz regime.

34 Our method reproduces the spectrally and spatially resolved absolute photon count rates.
 35 This is demonstrated on an experiment with idler photons in the terahertz range and signal
 36 photons in the visible range. The extreme wavelength spread between signal and idler leads
 37 to a setup that covers a large range in frequency and emission directions and further has
 38 multiple quasi-phasematching (QPM) orders overlapping in the same wavelength range. In
 39 the terahertz range additional processes such as parametric up- and (nonspontaneous) down-
 40 conversion occur parallel to SPDC. In order to adequately match the experimental data we
 41 include these processes in our simulation. The high qualitative and quantitative agreement
 42 with experimental results demonstrates the capabilities of our simulation method even for
 43 complex SPDC sources.

44 2 Theory

45 Our model is based on the second-order nonlinear interaction of electromagnetic fields to-
 46 gether with a first-order perturbation theory approximation. We start with the Hamiltonian [17]

47

$$H_{\text{NL}}(t) = \frac{1}{3} \epsilon_0 \int d\mathbf{r} \zeta_{jkl}^{(2)}(\mathbf{r}) \mathbf{D}_j(\mathbf{r}, t) \mathbf{D}_k(\mathbf{r}, t) \mathbf{D}_l(\mathbf{r}, t), \quad (1)$$

48 where $\zeta_{jkl}^{(2)}$ is the second-order inverse susceptibility tensor and \mathbf{D} are the displacement fields.
 49 This formulation is necessary to ensure consistency after quantization [18, 19].

50 We describe the pump beam as a classical monochromatic Gaussian beam with linear po-
 51 larization. We assume that the pump is undepleted. In addition, we use the approximation of
 52 a collimated beam such that the curvature and the Gouy phase can be neglected. The pump
 53 propagates along the z-axis, which we define parallel to the optical axis of the system. The
 54 signal and idler fields are described using a plane-wave decomposition separated into positive
 55 and negative frequency components $\hat{\mathbf{D}}^+$ and $\hat{\mathbf{D}}^-$ with

$$\hat{\mathbf{D}}^+(\mathbf{r}, t) = \sum_{\mathbf{k}, \sigma} i \sqrt{\frac{\epsilon_0 n_{\mathbf{k}}^2 \hbar \omega_{\mathbf{k}}}{2V}} \hat{a}_{\mathbf{k}, \sigma} \epsilon_{\mathbf{k}, \sigma} e^{i(\mathbf{k} \cdot \mathbf{r} + \omega_{\mathbf{k}} t)}, \quad (2)$$

56 and $\hat{\mathbf{D}}^-$ being the hermitian conjugate of $\hat{\mathbf{D}}^+$. Here, V is the quantization volume, $\hat{a}_{\mathbf{k}, \sigma}$ is
 57 the annihilation operator for a photon with momentum \mathbf{k} , and $\epsilon_{\mathbf{k}, \sigma}$ is the direction of the
 58 displacement field vector indexed with the polarization σ .

59 We then approximate the two-photon state $|\psi(t)\rangle$ using first-order perturbation theory.
 60 Under the assumption that the quantization volume is large, we can make a transition from
 61 sums to integrals in Eq. (2). From this we obtain the signal count rate density:

$$\Gamma_d(\mathbf{k}_s) = \frac{1}{T_1} \langle \psi(T_1) | \hat{a}^\dagger(\mathbf{k}_s) \hat{a}(\mathbf{k}_s) | \psi(T_1) \rangle \quad (3)$$

$$= Z \sum_{\sigma_s, \sigma_i} \sum_{m \text{ odd}} \int dk_1^3 \|A(\mathbf{k}_s, \mathbf{k}_i)\|^2, \quad (4)$$

62 with

$$A(\mathbf{k}_s, \mathbf{k}_i) = \frac{\chi_{\text{eff}}^{(2)}}{m} \sqrt{\frac{\omega_s \omega_i}{n_s^2 n_i^2}} \text{sinc}\left[\frac{1}{2} \Delta k_z L\right] \exp\left[-\frac{1}{4} (\Delta k_x^2 + \Delta k_y^2) w_p^2\right] \text{sinc}\left[\frac{1}{2} \Delta \omega T_1\right]$$

63 and

$$Z = \frac{16Pw_p^2L^2T_I}{(2\pi)^7\epsilon_0n_pc}. \quad (5)$$

64 Here T_I is the interaction time for a pump photon with the nonlinear medium, m denotes
 65 the odd QPM orders, and we sum over permutations of the indices j, k, l and substitute new
 66 indices to denote pump (p), signal (s) and idler (i). $\Delta k_z = \mathbf{k}_{pz} - \mathbf{k}_{sz} - \mathbf{k}_{iz} + k_\Lambda$ and $\Delta k_j = \mathbf{k}_{sj} + \mathbf{k}_{ij}$
 67 with $j = x, y$ are the longitudinal and transversal phase mismatches, and $\Delta\omega = \omega_p - \omega_s - \omega_i$
 68 corresponds to the energy mismatch. The width of the transverse part is determined by the
 69 waist radius w_p of the pump beam. The periodic poling offset $k_\Lambda = 2m\pi/\Lambda$ depends on
 70 the poling period of the crystal Λ and the QPM order m . P denotes the power of the pump
 71 beam and L the length of the crystal. The refractive indices n and $\chi_{\text{eff}}^{(2)}$ are functions of the
 72 wave vectors $\mathbf{k}_p, \mathbf{k}_s, \mathbf{k}_i$ and their corresponding polarizations. The spectral dependence of
 73 the nonlinear coefficient is modeled with Miller's rule [20]. The spatial variation of $\chi_{\text{eff}}^{(2)}$ is
 74 considered by calculating the effective value from the tensor components and displacement
 75 field directions [21]. Spatial variation in the refractive indices is considered following [22].
 76 The spectral dependencies are especially relevant since we simulate a large spectral range in
 77 the terahertz regime, from ~ 0.1 THz to 3.6 THz. The spatial variation cannot be neglected
 78 here, because the transverse momentum conservation dictates a large emission angle range
 79 for the idler photons.

80 With the idler in the terahertz range, at room temperature, thermal photons at the idler
 81 wavelength have to be taken into account [23]. These thermal photons interact with the pump
 82 laser as well. Through parametric down-conversion, additional photons at the signal wave-
 83 length are created. We derive this process analogously to SPDC. Instead of an initial vacuum
 84 state we have a thermal state for the idler. This leads to the same phasematching properties,
 85 but instead of a "1" from the vacuum fluctuations we obtain the thermal fluctuations

$$N_{\text{th}} = \frac{1}{\exp(\hbar\omega_i/k_B T_c) - 1}, \quad (6)$$

86 where T_c is the temperature of the crystal. The influence of thermal fluctuations for the signal
 87 can be neglected.

88 The emitted spectrum is propagated from the crystal onto a detector through an optical
 89 system. The number of counts for a single detector pixel is obtained by integrating over all
 90 signal wave vectors that are propagated to this pixel. However, not all photons created in the
 91 crystal arrive at the detector. We consider the losses from internal reflection in the crystal,
 92 during propagation through the optical setup and the efficiency of the detector summarized
 93 into a single factor η . With this we obtain the photon counts for the detector pixel with
 94 indices (i, j)

$$R_d^{(i,j)} = \eta T (1 + N_{\text{th}}) \int_{\Omega(i,j)} d\mathbf{k}_s \Gamma_d(\mathbf{k}_s), \quad (7)$$

95 where T is the illumination time of the detector and $\Omega(i, j)$ is defined such that every ray with
 96 $\mathbf{k}_\Omega \in \Omega(i, j)$ at the crystal exit is propagated through the optical system onto the detector pixel
 97 (i, j) . Along the same lines we obtain the rate for the parametric up-conversion process, where
 98 a thermal photon and a laser photon merge into a signal photon. The only changes are the
 99 signs of the terahertz frequency ω_i in the terms $\Delta\omega$ and the wave vector \mathbf{k}_j in the respective
 100 Δk_j terms with $j = x, y, z$. Up-conversion is only caused by thermal fluctuations, such that
 101 the up-conversion rate is given by:

$$R_u^{(i,j)} = \eta T N_{\text{th}} \int_{\Omega(i,j)} d\mathbf{k}_s \Gamma_u(\mathbf{k}_s). \quad (8)$$

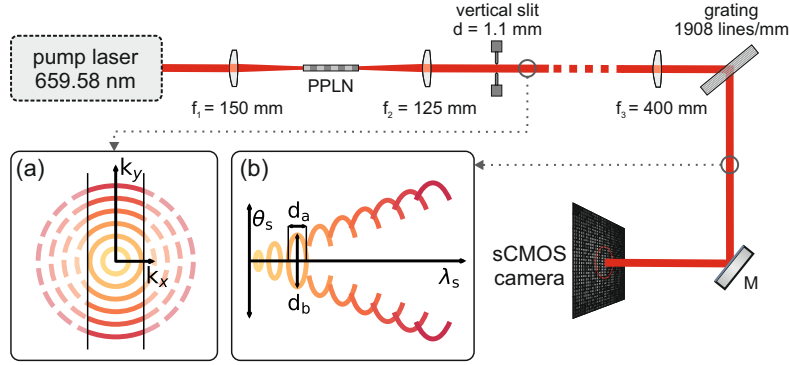


Figure 1: Layout of the experimental setup. Only the components used in the simulations are included. f : lens. PPLN: periodically poled MgO-doped LiNbO₃-crystal. M: mirror. Length of optical paths are not to scale. (a) represents a cross section of the spectrum after the slit. (b) sketches the separation of spectral components by the grating. The ratio d_a/d_b quantifies the asymmetry introduced in this step.

102 2.1 Simulated Setup

103 A sketch of the model for the experimental setup is shown in Fig. 1, where only the simulated
 104 components are shown. The setup consists of a narrow bandwidth laser, a nonlinear crystal
 105 and an imaging system. The spatial and spectral components of the created signal photons are
 106 separated by the imaging system and imaged onto the detector. The imaging system contains
 107 a slit to limit the transmission of rays with large k_x , shown in Fig. 1 (a), resulting in a sharper
 108 image on the detector. This effect is shown in Fig. 1 (b), where the remaining parts of the
 109 ellipses are separated along the θ_s axis. A transmission grating separates the spectral compo-
 110 nents of the photons. Photons with a fixed wavelength are emitted in a cone shape, shown in
 111 Fig. 1 (a). This leads to an imperfect separation of spatial and spectral components, which is
 112 shown by the full and partial ellipses in Fig. 1 (b). The ratio d_a/d_b is a measure of how much
 113 an ellipse is squeezed. As it approaches zero, the ellipses are imaged as vertical lines, making
 114 the spread in θ_s large and the one in λ_s small. The system further contains several filters and
 115 Bragg gratings to suppress the pump radiation that are not considered in this model. A detailed
 116 description of the experimental realization is given by Haase *et al.* [24]. The laser is modeled
 117 with a wavelength of $\lambda_p = 659.58$ nm and a beamwaist $w_p = 43$ μm . The nonlinear crystal
 118 is a periodically poled MgO-doped lithium niobate crystal with dimensions $5 \times 1 \times 10$ mm³
 119 ($H \times W \times L$) and a poling period of 170 μm . Due to symmetries in the nonlinear susceptibility
 120 only the values of the $\chi_{333}^{(2)}$ and $\chi_{311}^{(2)}$ components need to be considered. The $\chi_{222}^{(2)}$ component
 121 is not relevant to any processes in our setup. We use a value of $\chi_{333}^{(2)} = 327$ pm/V at 661 nm
 122 and 0.75 THz which we obtained from a fit to the experimental results. The fitted $\chi_{333}^{(2)}$ value
 123 agrees with a scaled value from the infrared range [25] but is ~ 1.5 times larger than other
 124 scaled values from the terahertz range [26, 27]. The difference can be explained by different
 125 factors for the Hamiltonian ($\frac{1}{2}$ and $\frac{1}{3}$) used in the classical and quantum approaches. Com-
 126 pared to our previous estimation [24] this value is two times larger. There are two reasons
 127 for this: First, we did not use Miller's rule in the previous method, but assumed a constant
 128 value. Second, we added the full optical model to the simulation, which changes the shape
 129 of the spectrum. The value of $\chi_{311}^{(2)} = 49$ pm/V at 661 nm and 0.75 THz is a scaled value
 130 from [25]. The contributions of this parameter are small such that a reliable fit is not possible.
 131 The refractive indices, for ~ 5 mol.% MgO-doped LiNbO₃, are taken from [28, 29].

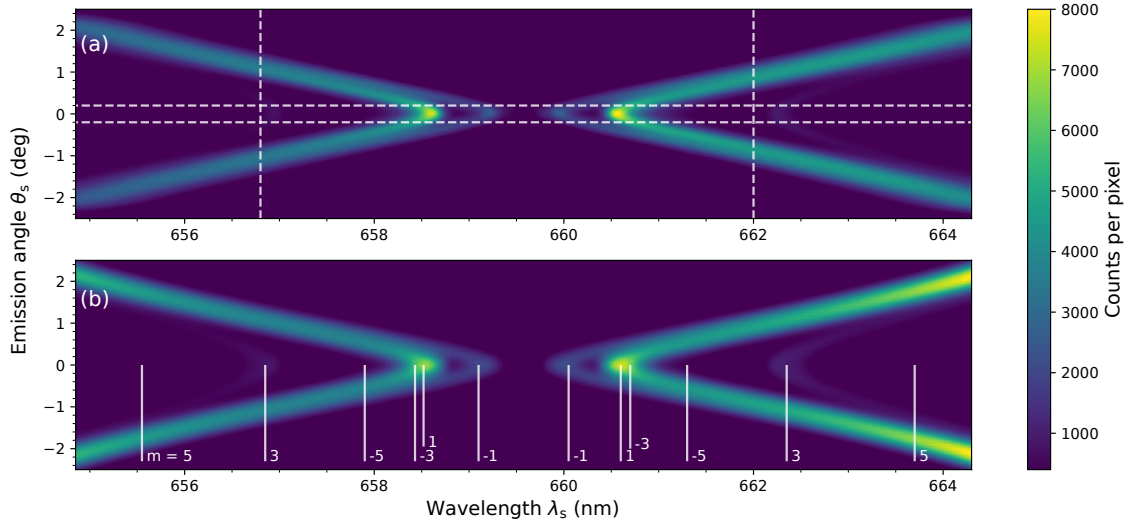


Figure 2: Experimental (a) and simulated (b) frequency-angular spectrum. The average dark count rate is subtracted from the experimental spectrum. The dashed lines in (a) denote the location of the cuts presented in Fig. 3 and 4. The numbers m in (b) indicate the contributions of the different QPM orders. The tails on the left correspond to up-conversion, the ones on the right to down-conversion.

132 2.2 Optical Propagation

133 The propagation through the optical system is modeled by paraxial ray optics assuming ideal
 134 optical components. The paraxial approximation is reasonable as only the signal photons are
 135 detected. The idler photons which are emitted at larger angles are not considered. Since the
 136 longitudinal positions of the optical components are not exactly known, they are estimated
 137 from the imaging properties of the setup. This is done using numerical optimization to min-
 138 imize the squared difference of three experimentally measured values: the transformation of
 139 wavelength into a position on the x-axis, the relation between emission angle and position on
 140 the y-axis, and the squeezing of a monochromatic circular beam, defined by the ratio d_a/d_b .
 141 We also penalize deviations from the measured positions. This procedure of estimating the
 142 parameters of the setup mimics the alignment process performed in the experiment, where
 143 the components are moved around their nominal positions to obtain a sharper image. The
 144 calculated values deviate from the nominal distances of the setup, but reproduce the imag-
 145 ing properties of the actual experiment. Further sources of errors in the optical system such as
 146 misalignment transverse to the optical axis or deviations from nominal values are not included
 147 in our model.

148 2.3 Numerical Methods

149 We employ a Monte-Carlo integration scheme to evaluate the integrals in Eq. (3), approxi-
 150 mating each squared sinc functions with the sum of three scaled Gaussians. This allows for
 151 efficient sampling while maintaining a small error in the approximated function. Other ap-
 152 proximations [10, 30] are either less accurate or less efficient. The sum in Eq. (3) is evalu-
 153 ated up to the seventh QPM order. Since positive and negative orders are possible, a total of
 154 eight summands are evaluated. Higher orders contribute less than 70 counts per pixel to the
 155 spectrum in the observed range and are therefore neglected. We consider both ordinary and
 156 extraordinary polarization for signal and idler. Type 0 parametric conversion contributes most
 157 of the spectrum in the investigated range, type I contributes less than 165 counts per pixel in

158 the region above 663.7 nm and less than 2 counts per pixel elsewhere. Type II contributes less
 159 than 1 count per pixel in the whole range.

160 3 Results

161 The experimental and numerical results for the full spectrum are shown in Fig. 2. The exper-
 162 imental spectrum is a single image as recorded by the sCMOS camera with the average dark
 163 count rate subtracted. Simulated and experimental spectrum show four distinct tails for up-
 164 as well as down-conversion. The contributing QPM orders for each tail are given in panel
 165 (b) of the figure. The tails corresponding to the fifth QPM order are barely visible, while the
 166 contributions of the seventh order cannot be distinguished at all due to the lower conversion
 167 efficiency of higher orders. The experiment is limited to a scattering angle of around $\pm 2.3^\circ$ by
 168 the apertures of the optical components. The simulated spectrum extends beyond this angle
 169 as the limiting apertures are not included in the model.

170 The simulation shows more counts than the experiment at wavelengths lower than 655 nm
 171 and higher than 663.5 nm for up- and down-conversion, respectively. Potential reasons are
 172 limiting apertures in the experiment or an incorrect model for the terahertz refractive indices.
 173 The idler photons in this range have a frequency of over 2.5 THz which is beyond the measured
 174 range of our reference, covering frequencies from 0.3 THz to 1.9 THz. The value of $\chi_{\text{eff}}^{(2)}$
 175 depends on the refractive indices in our model such that an overestimation of n increases the
 176 counts.

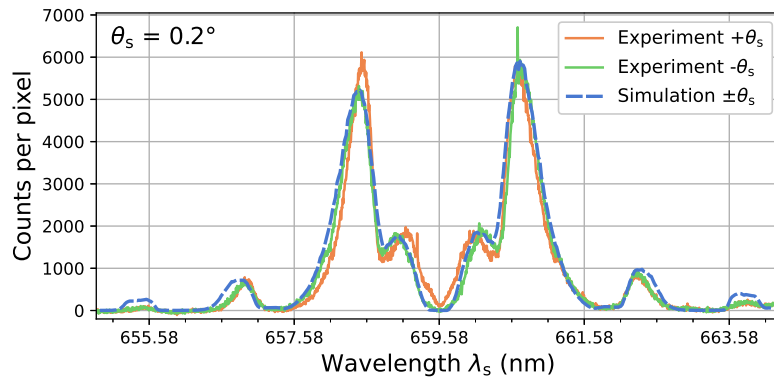


Figure 3: Horizontal cut through the experimental and simulated spectra at $\theta_s = 0.2^\circ$. The positive and negative sign for θ_s correspond to cuts through the upper and lower half of Fig. 2 respectively. The simulated spectrum is symmetric in θ_s , thus only one line is shown.

177 Figures 3 and 4 show horizontal and vertical cuts of the spectrum. The positive and nega-
 178 tive values for θ_s correspond to the sign given in Fig. 2. As the simulated spectrum is symmetric
 179 in θ_s only one line is shown. Both cuts show good agreement in position, width and height
 180 of the peaks. The experimental spectrum shows some remaining pump light around the laser
 181 wavelength at the center of Fig. 3. This is more pronounced for the $+\theta_s$ case. In the model we
 182 assume the pump to be blocked completely, therefore the simulated spectrum does not show
 183 the pump rest.

184 The tails of the experimental spectrum are slightly narrower and more pronounced, which
 185 is due to the experiment being adjusted for a maximally sharp image, while the simulated setup
 186 is not. It is optimized to reproduce three imaging characteristics of the experiment. Observed
 187 differences between simulation and experiment are of the same order of magnitude as the

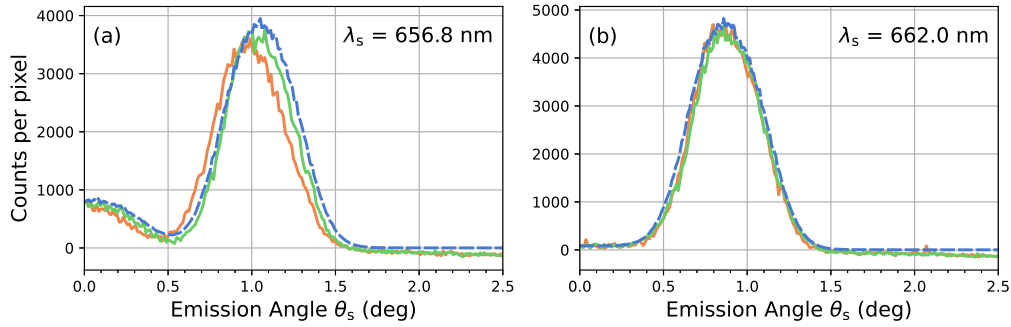


Figure 4: Vertical cuts through the experimental and simulated spectra. Panel (a) shows a cut in the up-conversion regime, panel (b) in the down-conversion regime. The color coding is the same as in Fig. 3.

188 differences between the two experimental results. Peaks found in the cuts from larger angles
 189 or larger wavelengths match in shape and position. The peaks of the simulated spectrum are
 190 significantly higher for this region. Note that the simulated spectrum exhibits some minor
 191 modulation along the θ_s -axis which are numerical artifacts caused by the employed sampling
 192 method.

193 4 Conclusion

194 The demonstrated simulation of parametric conversion spectra shows good agreement with the
 195 experiment in spectral and angular distributions as well as absolute photon counts. Qualitative
 196 and quantitative features of the experimentally obtained spectrum can be reproduced. Vari-
 197 ous effects such as SPDC, the influence of thermal photons and parametric up-conversion were
 198 simulated. This shows the potential of applying our model to predict accurate characteristics
 199 of photon sources. And the possibility of identifying the contributions of different processes.
 200 The model can be simplified for faster computation times. An important step to improve the
 201 simulation results is to use better estimates for the crystal characteristics in the investigated
 202 frequency range. The method provides significant benefits over traditional methods such as
 203 the calculation of phasematching curves as no information about the width or intensity of
 204 the spectrum is provided there. Our numerical method also allows for reconstruction of the
 205 spectrum at the crystal face which allows to investigate spatial, spectral and correlation prop-
 206 erties without the need of building optical setups for measuring them. Compared to previous
 207 results [24], the propagation of the spectrum through the measurement setup improves the
 208 simulation results. Further research is needed to separate influences of model errors in the
 209 up- and down-conversion model from those in the optical measurement setup. Nonetheless,
 210 the presented model provides the necessary basis for the simulation of many quantum optic
 211 applications such as quantum imaging.

212 **Funding information** Fraunhofer-Gesellschaft (Lighthouse project QUILT)

213 References

214 [1] T. B. Pittman, Y. H. Shih, D. V. Strekalov and A. V. Sergienko, *Optical imaging*
 215 *by means of two-photon quantum entanglement*, Phys. Rev. A **52**, R3429 (1995),

- 216 doi:[10.1103/PhysRevA.52.R3429](https://doi.org/10.1103/PhysRevA.52.R3429).
- 217 [2] M. J. Padgett and R. W. Boyd, *An introduction to ghost imaging: quantum and classical*,
218 Philosophical Transactions of the Royal Society A: Mathematical, Physical and Engineer-
219 ing Sciences **375**(2099), 20160233 (2017), doi:[10.1098/rsta.2016.0233](https://doi.org/10.1098/rsta.2016.0233).
- 220 [3] A. Vanselow, P. Kaufmann, I. Zorin, B. Heise, H. M. Chrzanowski and S. Ramelow,
221 *Frequency-domain optical coherence tomography with undetected mid-infrared photons*,
222 Optica **7**(12), 1729 (2020), doi:[10.1364/OPTICA.400128](https://doi.org/10.1364/OPTICA.400128).
- 223 [4] C. Lindner, J. Kunz, S. J. Herr, S. Wolf, J. Kießling and F. Kühnemann, *Nonlinear interfer-*
224 *ometer for fourier-transform mid-infrared gas spectroscopy using near-infrared detection*,
225 Opt. Express **29**(3), 4035 (2021), doi:[10.1364/OE.415365](https://doi.org/10.1364/OE.415365).
- 226 [5] M. Kutas, B. Haase, J. Klier, D. Molter and G. von Freymann, *Quantum-*
227 *inspired terahertz spectroscopy with visible photons*, Optica **8**(4), 438 (2021),
228 doi:[10.1364/OPTICA.415627](https://doi.org/10.1364/OPTICA.415627).
- 229 [6] M. Kutas, B. Haase, P. Bickert, F. Riexinger, D. Molter and G. von Frey-
230 mann, *Terahertz quantum sensing*, Science Advances **6**(11), eaaz8065 (2020),
231 doi:[10.1126/sciadv.aaz8065](https://doi.org/10.1126/sciadv.aaz8065).
- 232 [7] G. B. Lemos, V. Borish, G. D. Cole, S. Ramelow, R. Lapkiewicz and A. Zeilinger,
233 *Quantum imaging with undetected photons*, Nature **512**(7515), 409 (2014),
234 doi:[10.1038/nature13586](https://doi.org/10.1038/nature13586).
- 235 [8] J. Fuenzalida, A. Hochrainer, G. B. Lemos, E. A. Ortega, R. Lapkiewicz, M. Lahiri and
236 A. Zeilinger, *Resolution of Quantum Imaging with Undetected Photons*, Quantum **6**, 646
237 (2022), doi:[10.22331/q-2022-02-09-646](https://doi.org/10.22331/q-2022-02-09-646).
- 238 [9] M. Gilaberte Basset, A. Hochrainer, S. Töpfer, F. Riexinger, P. Bickert, J. R. León-Torres,
239 F. Steinlechner and M. Gräfe, *Video-rate imaging with undetected photons*, Laser & Pho-
240 tonics Rev. **15**(6), 2000327 (2021), doi:[10.1002/lpor.202000327](https://doi.org/10.1002/lpor.202000327).
- 241 [10] J. Schneeloch and J. C. Howell, *Introduction to the transverse spatial correlations in*
242 *spontaneous parametric down-conversion through the biphoton birth zone*, J. Opt. **18**(5),
243 053501 (2016), doi:[10.1088/2040-8978/18/5/053501](https://doi.org/10.1088/2040-8978/18/5/053501).
- 244 [11] S. Trajtenberg-Mills, A. Karnieli, N. Voloch-Bloch, E. Megidish, H. S. Eisenberg and
245 A. Arie, *Simulating correlations of structured spontaneously down-converted photon pairs*,
246 Laser & Photonics Rev. **14**(3), 1900321 (2020), doi:[10.1002/lpor.201900321](https://doi.org/10.1002/lpor.201900321).
- 247 [12] R. S. Bennink, *Optimal collinear gaussian beams for spontaneous parametric down-*
248 *conversion*, Phys. Rev. A **81**, 053805 (2010), doi:[10.1103/PhysRevA.81.053805](https://doi.org/10.1103/PhysRevA.81.053805).
- 249 [13] R. S. Bennink, Y. Liu, D. D. Earl and W. P. Grice, *Spatial distinguishability of photons*
250 *produced by spontaneous parametric down-conversion with a focused pump*, Phys. Rev. A
251 **74**, 023802 (2006), doi:[10.1103/PhysRevA.74.023802](https://doi.org/10.1103/PhysRevA.74.023802).
- 252 [14] C. I. Osorio, G. Molina-Terriza, B. G. Font and J. P. Torres, *Azimuthal distinguishability*
253 *of entangled photons generated in spontaneous parametric down-conversion*, Opt. Express
254 **15**(22), 14636 (2007), doi:[10.1364/OE.15.014636](https://doi.org/10.1364/OE.15.014636).
- 255 [15] Z. Zhao, K. A. Meyer, W. B. Whitten, R. W. Shaw, R. S. Bennink and W. P. Grice, *Observation*
256 *of spectral asymmetry in cw-pumped type-ii spontaneous parametric down-conversion*, Phys.
257 Rev. A **77**, 063828 (2008), doi:[10.1103/PhysRevA.77.063828](https://doi.org/10.1103/PhysRevA.77.063828).

- 258 [16] R. Ramírez-Alarcón, H. Cruz-Ramírez and A. B. U'Ren, *Effects of crystal length on the*
259 *angular spectrum of spontaneous parametric downconversion photon pairs*, *Laser Phys.*
260 **23**(5), 055204 (2013), doi:[10.1088/1054-660x/23/5/055204](https://doi.org/10.1088/1054-660x/23/5/055204).
- 261 [17] J. Schneeloch, S. H. Knarr, D. F. Bogorin, M. L. Levangie, C. C. Tison, R. Frank, G. A.
262 Howland, M. L. Fanto and P. M. Alsing, *Introduction to the absolute brightness and num-*
263 *ber statistics in spontaneous parametric down-conversion*, *J. Opt.* **21**(4), 043501 (2019),
264 doi:[10.1088/2040-8986/ab05a8](https://doi.org/10.1088/2040-8986/ab05a8).
- 265 [18] M. Hillery and L. D. Mlodinow, *Quantization of electrodynamics in nonlinear dielectric*
266 *media*, *Phys. Rev. A* **30**, 1860 (1984), doi:[10.1103/PhysRevA.30.1860](https://doi.org/10.1103/PhysRevA.30.1860).
- 267 [19] N. Quesada and J. E. Sipe, *Why you should not use the electric field to quantize in nonlinear*
268 *optics*, *Opt. Lett.* **42**(17), 3443 (2017), doi:[10.1364/OL.42.003443](https://doi.org/10.1364/OL.42.003443).
- 269 [20] R. C. Miller, *Optical second harmonic generation in piezoelectric crystals*, *Appl. Phys. Lett.*
270 **5**(1), 17 (1964), doi:[10.1063/1.1754022](https://doi.org/10.1063/1.1754022).
- 271 [21] R. W. Boyd, *Nonlinear Optics*, Academic Press, Inc., USA, 3rd edn., ISBN 0123694701,
272 doi:[10.1016/B978-0-12-369470-6.00001-0](https://doi.org/10.1016/B978-0-12-369470-6.00001-0) (2008).
- 273 [22] M. Born and E. Wolf, *Principles of Optics: Electromagnetic Theory of Propagation, Interfer-*
274 *ence and Diffraction of Light*, Cambridge University Press, 60th anniversary edition edn.,
275 ISBN 9781139644181, doi:[10.1017/CBO9781139644181](https://doi.org/10.1017/CBO9781139644181) (2019).
- 276 [23] G. K. Kitaeva, S. Kovalev, A. Penin, A. Tuchak and P. Yakunin, *A method of calibration of*
277 *terahertz wave brightness under nonlinear-optical detection*, *J. Infrared Millim. Terahertz*
278 *Waves* **32**(10), 1144 (2011), doi:[10.1007/s10762-011-9780-y](https://doi.org/10.1007/s10762-011-9780-y).
- 279 [24] B. Haase, M. Kutas, F. Riexinger, P. Bickert, A. Keil, D. Molter, M. Bortz and G. von
280 Freymann, *Spontaneous parametric down-conversion of photons at 660 nm to the*
281 *terahertz and sub-terahertz frequency range*, *Opt. Express* **27**(5), 7458 (2019),
282 doi:[10.1364/OE.27.007458](https://doi.org/10.1364/OE.27.007458).
- 283 [25] D. N. Nikogosyan, *Nonlinear optical crystals: a complete survey*, Springer Science &
284 Business Media, ISBN 978-0-387-22022-2, doi:[10.1007/b138685](https://doi.org/10.1007/b138685) (2006).
- 285 [26] J. Hebling, A. G. Stepanov, G. Almási, B. Bartal and J. Kuhl, *Tunable THz pulse generation*
286 *by optical rectification of ultrashort laser pulses with tilted pulse fronts*, *Appl. Phys. B* **78**(5),
287 593 (2004), doi:[10.1007/s00340-004-1469-7](https://doi.org/10.1007/s00340-004-1469-7).
- 288 [27] K. Vodopyanov, *Optical THz-wave generation with periodically-inverted GaAs*, *Laser &*
289 *Photonics Rev.* **2**(1-2), 11 (2008), doi:[10.1002/lpor.200710028](https://doi.org/10.1002/lpor.200710028).
- 290 [28] X. Wu, C. Zhou, W. R. Huang, F. Ahr and F. X. Kärtner, *Temperature dependent refractive*
291 *index and absorption coefficient of congruent lithium niobate crystals in the terahertz range*,
292 *Opt. Express* **23**(23), 29729 (2015), doi:[10.1364/OE.23.029729](https://doi.org/10.1364/OE.23.029729).
- 293 [29] O. Gayer, Z. Sacks, E. Galun and A. Arie, *Temperature and wavelength dependent refractive*
294 *index equations for MgO-doped congruent and stoichiometric LiNbO₃*, *Appl. Phys. B* **91**(2),
295 343 (2008), doi:[10.1007/s00340-008-2998-2](https://doi.org/10.1007/s00340-008-2998-2).
- 296 [30] P. Kolenderski, W. Wasilewski and K. Banaszek, *Modeling and optimization of photon*
297 *pair sources based on spontaneous parametric down-conversion*, *Phys. Rev. A* **80**, 013811
298 (2009), doi:[10.1103/PhysRevA.80.013811](https://doi.org/10.1103/PhysRevA.80.013811).